Journal of Colloid and Interface Science 677 (2025) 171–180

Contents lists available at ScienceDirect

Journal of Colloid And Interface Science

journal homepage: www.elsevier.com/locate/jcis

Regular Article

Artificial chemotaxis under electrodiffusiophoresis

Carlos A. Silvera Batista [a,b], Kun Wang [a], Hannah Blake [a], Vivian Nwosu-Madueke [a], Sophie Marbach [c,*]

[a] Department of Chemical and Biomolecular Engineering, Vanderbilt University, Nashville, 37205, United States
[b] Vanderbilt Institute for Nanoscale Science and Engineering, Vanderbilt University, Nashville, 37205, United States
[c] CNRS, Sorbonne Université, Physicochimie des Electrolytes et Nanosystèmes Interfaciaux, Paris, F-75005, France

GRAPHICAL ABSTRACT

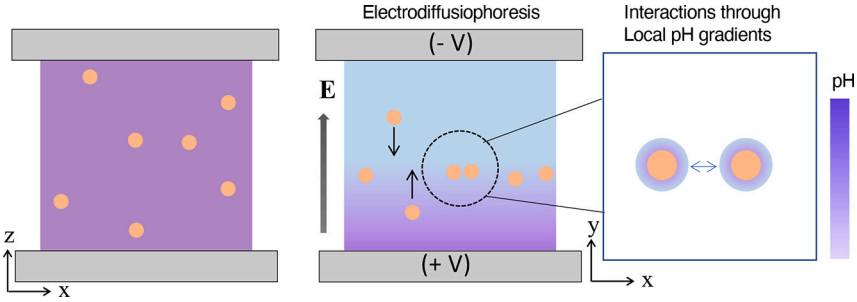

ARTICLE INFO

Keywords:
Diffusiophoresis
Chemotaxis
Self-assembly
Non-reciprocal interactions
Electrophoresis

ABSTRACT

Hypothesis: Through a large parameter space, electric fields can tune colloidal interactions and forces leading to diverse static and dynamical structures. So far, however, field-driven interactions have been limited to dipole-dipole and hydrodynamic contributions. Nonetheless, in this work, we propose that under the right conditions, electric fields can also induce interactions based on local chemical fields and diffusiophoretic flows.

Experiments: Herein, we present a strategy to generate and measure 3D chemical gradients under electric fields. In this approach, faradaic reactions at electrodes induce *global* pH gradients that drive long-range transport through electrodiffusiophoresis. Simultaneously, the electric field induces *local* pH gradients by driving the particle's double layer far from equilibrium.

Findings: As a result, while global pH gradients lead to 2D focusing away from electrodes, local pH gradients induce aggregation in the third dimension. Evidence points to a mechanism of interaction based on diffusiophoresis. Interparticle interactions display a strong dependence on surface chemistry, zeta potential and diameter of particles. Furthermore, pH gradients can be readily tuned by adjusting the voltage and frequency of the electric field. For large Péclet numbers, we observed a collective chemotactic-like collapse of particles. Remarkably, such collapse occurs without reactions at a particle's surface. By mixing particles with different sizes, we also demonstrate, through experiments and Brownian dynamics simulations, the emergence of non-reciprocal interactions, where small particles are more drawn towards large ones.

* Corresponding author.
E-mail addresses: silvera.batista@vanderbilt.edu (C.A. Silvera Batista), sophie.marbach@cnrs.fr (S. Marbach).

https://doi.org/10.1016/j.jcis.2024.08.004
Received 16 April 2024; Received in revised form 30 July 2024; Accepted 1 August 2024
Available online 6 August 2024

1. Introduction

Migration of cells along chemical gradients, *chemotaxis*, constitutes an essential mechanism of adaptation, that serves to mount an immune response or to sustain embryonic development [84,14]. To navigate a chemical landscape, cells rely on the active generation, detection, transmission and transduction of chemical signals [68]. Interestingly, the same principles can be replicated through purely physical mechanisms, such as diffusiophoresis (DP) [3]. DP refers to the directed, yet passive, transport of colloidal particles and macromolecules in response to concentration gradients of solutes [17,4,57,42,70,67]. Particles "sense" solute gradients through surface-solute interactions, which build up fluid pressure and induce flows.

DP constitutes a versatile form of colloidal transport because it enables control of motion by tuning properties of particles and gradients of solutes. Consequently, interest in DP has increased over the last 15 years for applications in separation [72,25], transport in porous media [34,73], detergency [74,90], drug delivery [32], desalination [28,58], decontamination [26], and patterning [1]. Fascinatingly, DP is also harnessed by cells to transport cargos [61] or to navigate chemical gradients [19], undergoing sometimes both DP and chemotaxis [70].

External and global chemical gradients can be generated through many mechanisms [82], such as chemical reactions [52,13], mineral dissolution [45], and molecular exclusion [25,50]. Lately, solute-inertial beacons, which release solutes continuously, have facilitated the study of long-range DP [8,7,50,51]. Solute-inertial beacons impose deterministic—attractive or repulsive—forces over long distances, $\gg 1$ μm [51,6]. In contrast, local chemical fields can arise when microparticles act as sinks or sources of solutes. For example, photocatalytic reactions on the surface of particles promote on-demand colloidal phase separation [48,44], with applications in optical camouflage [96]. For particles with broken symmetry, anisotropic consumption of solutes induces phoretic self-propulsion [47], and rich collective dynamics, exemplified by motility-induced phase separation, chemotactic collapse or gel-like phases [21,79,56]. All the systems above require a solute playing the role of a slowly consumed fuel; therefore, solute gradients are hard to sustain for long times.

Despite diverse existing strategies to induce local and global chemical gradients, studies on DP mostly focus on solute gradients that are either in 1D geometries, or that emanate radially from a beacon or particle. Nonetheless, recent studies reveal that unconventional geometries open new opportunities for complex manipulation of colloids, such as spatial and temporal design of 2D diffusiophoretic banding [60], as well as solenoidal currents for long-range transport [89,91].

Although much less explored, AC electric fields can promote conditions for diffusiophoretic transport in two ways. At low frequencies, electric fields drive electrochemical reactions that induce gradients of electroactive species. Charged particles respond to such gradients by moving under electrodiffusiophoresis (EDP)—a combination of diffusiophoresis and electrophoresis [81,63,80,26,85]. In previous works, we demonstrated that uniform AC electric fields can effect long-range directional transport under EDP [86]. On the other hand, in addition to electric potential and velocity of the fluid, electric fields can perturb concentration of electrolytes near a charged particle. Perturbation of these variables results in electric dipoles, electrohydrodynamic (EHD) flows and concentration polarization [38]. The effect of dipole-dipole [95,10,69] and hydrodynamic interactions [64,39,88] on assembly has been established over the last 20 years. However, much less attention has been devoted to understanding how induced *local* gradients of electrolyte affect interparticle interactions. Work in the former Soviet Union by A. S. Dukhin and collaborators predicted that formation of diffusion layers surrounding particles could mediate interactions through diffusiophoresis [27], while recent publications have brought attention to nonlinear electrokinetic effects due to concentration polarization [35,23]; thus, raising the possibility that induced local gradients may drive interparticle interactions.

In this paper, we demonstrate conditions where diffusiophoretic contributions to interparticle interactions become dominant under AC electric fields. Using low-frequency AC fields ($\lesssim 2$ kHz), we induce *global* pH gradients that lead to long-range transport and focusing of charged particles on a plane far from electrodes [85,86]. Once at the focusing plane, *local* pH gradients around particles result in long-range in-plane attraction and "artificial" chemotaxis. Remarkably, we induce local chemical fields without fuel consumption at a particle's surface, therefore establishing an important difference with the state of the art of active particles. Instead, pH gradients result from driving the electrical double layer, and its surroundings, far from equilibrium. Local pH gradients depend on properties of particles, such as surface chemistry, zeta potential, and diameter. These gradients can be easily tuned via frequency and amplitude of the applied AC electric field. Under some conditions, we observe collective aggregation reminiscent of chemotactic collapse and non-reciprocal interactions (meaning two different particles are attracted to one another in different ways). This diversity of behavior unlocks a broad set of possibilities to engineer diffusiophoresis by externally-controlled electric fields.

2. Materials and methods

The following paragraphs describe the procedures followed for preparation of materials, experimental setup and analysis.

Model systems

The model systems were fluorescent polystyrene particles (PS) with nominal diameters of 2 μm (Bangs Lab, FSPP005); fluorescent carboxyl-functionalized polystyrene particles (CB-PS) with nominal diameters of 1 μm (Bangs Lab, FCGB006), 1.75 μm (Polysciences, 17686) and 5 μm (Bangs Lab, FCGB008); and silica particles with nominal diameters of 2.3 μm (Spherotech, SIP-30-10). For the study of interparticle forces, all particles were dispersed in 100 μM solutions of SNARF-1 with a concentration of approximately 5×10^{-4}% w/v. Ultrapure deionized water (18 MΩ·cm) was used in all experiments. Measurements of zeta potential (ζ) were performed in a Litesizer 500 (Anton Paar) through electrophoretic light scattering. The particles used for experiments reported in Fig. 2 were negatively charged, with an average ζ value of -65.0 ± 3.1 mV for 1.75 μm CB-PS, -48.2 ± 4.4 for 2.0 μm PS, and -50.2 ± 5.5 for 2.3 μm silica particles. For studies reported in Fig. 3E, 5 μm CB-PS particles were modified by cross-linking poly(ethylene glycol) (PEG) chains of different molecular weights (5, and 10 kDa) to the carboxylate groups (PEG-modified particles, PEG-PS), following the procedure reported in reference [75]. Particles became less negatively charged after attachment of PEG molecules, with the magnitude of change modulated by the molecular weight of PEG. ζ for 10 kDa PEG-PS and 5 kDa PEG-PS particles were -46.2 ± 2.1 mV and -55.1 ± 1.9 mV, respectively.

Experimental setup

Fig. 1A shows a drawing of the experimental setup. The electrochemical cell was built by separating two indium tin oxide (ITO) coated glass slides (Diamond Coatings, 22×40 mm^2, 8–10 Ω per square) with a dielectric spacer with nominal thickness of 120 μm (9 mm diameter, Grace Biolabs, Cat. # 654002). The ITO slides were positioned such that ITO coatings were in contact with the suspension. Prior to each experiment, the slides were cleaned by sequentially sonicating them in acetone, isopropanol and DI water for 10 min in each solvent. Then, right before assembling the devices, the slides were treated with UV-ozone (UVO Cleaner Model 30, Jelight) for 10 min. In a typical experiment, approximately 10 μL of suspension was confined in the electrochemical cell. The AC electric fields were applied using a function generator (Rigol DG1022) with frequency ranging from 100 Hz to 10 kHz, and voltage varying from 1 to 5 Vpp (peak to peak). It is important to mention that we noticed a variability in the electrochemical response of ITO slides

from one batch to another; nonetheless, slides from the same batch behave almost identically. This was observed for slides from Diamond Coatings as well as SPI.

Particles, fluorescent dye, and electrodes were simultaneously imaged using a Leica SP8 Confocal Laser Scanning Microscope (CLSM). Water (40×, 1.10 NA) and oil (63×, 1.30 NA) immersion objectives were used, while the pinhole was set to 1 Airy unit. Optical properties of particles were selected to avoid significant overlap with the ratiometric dye (SNARF-1). Particles with absorption in the violet part of the spectrum were excited at 405 nm, and their emission was collected at wavelengths between 420 and 470 nm. A high-speed resonant scanner (8 kHz) enabled high acquisition rates of up to 28 frames per second at a resolution of 512 × 512 pixels. Two imaging modes were utilized. XYZT mode was used for observation within a given imaging volume, whereas XYT mode was used to image in xy plane at a given height. To measure pH around a single particle, imaging settings were optimized to balance acquisition speed with level of pixel-to-pixel noise. Once a single particle was located, images of approximately 17×17 μm^2 in size (with a zoom factor equal to 7, 40× water objective), were obtained with 512×512 pixel resolution, and with suitable frame and line averages. Videos of ten frames were acquired for ten different particles to quantify statistical significance. Further details on imaging can be found in SI Sec. 3. Before each experiment, the initial pH was adjusted to 7.1 by using aliquots of NaOH and HCl.

Measuring pH during operation

Details on measurements of pH in-operando can be found in our recent publication [86]. Briefly, pH was mapped by using a ratiometric fluorescense pH indicator, 5-(and-6)-carboxy SNARF-1 (ThermoFisher, C1270). SNARF-1 fluorescent emission presents a shift from yellow-orange to deep red with increasing pH, allowing pH to be obtained at any position through the ratio of emissions at two different wavelengths. Using the ratio of dual emission signals minimizes the effect of fluctuations in focus, excitation intensities, concentration of dye, and transmittance loss of ITO under electric field, thus proving a more reliable quantification of pH. In our experiments, SNARF-1 (100 μM) was excited at 514 nm, with detection of emission centered at 580 nm and 640 nm; in each case the spectral bandwidth was 10 nm. After acquisition of images, pH maps were calculated and plotted using an algorithm developed in Igor Pro, following the formula below:

$$\mathrm{pH} = \mathrm{pKa} - \log\left(\frac{\mathcal{R}_b - \mathcal{R}}{\mathcal{R} - \mathcal{R}_a} \cdot \frac{I_{b,2}}{I_{a,2}}\right). \tag{1}$$

$\mathcal{R}$ represents the ratio of emission intensities, I_1 (580 nm, yellow orange) and I_2 (640 nm, red), while $\mathcal{R}_b$ and $\mathcal{R}_a$ denote the ratio of intensities at the basic (I_b) and acidic (I_a) end points. The pH at every z-position was calculated by averaging the intensity of the whole frame for each channel. To quantify pH around particles, calculations were performed at every pixel of a single frame. To further improve the signal-to-noise ratio, we applied an average convolution filter with a kernel size equal to 5.

Data analysis

To obtain positions of particles from images, we detected the location of circles encapsulating particles, by adjusting size and intensity threshold in Matlab's "imfindcircles" function. Positions of particles were then obtained from the center of each circle. Trajectories and positions for the analysis of interparticle interactions in Fig. 1 were performed using the image analysis suite of the LAX S Leica software; in this software, we were able to use regions of interest to isolate dimers.

To obtain statistical properties from positions of particles we relied on standard definitions and algorithms. The pair distribution function $g(r)$ is defined as follows:

$$g(r) = \frac{\mathcal{A}}{2\pi r N} \sum_{i=1}^{N} \sum_{j \neq i} \delta(r - r_{ij}) \tag{2}$$

where N is the number of particles considered in an area $\mathcal{A}$, δ is the delta function, r is a distance from a reference particle, and r_{ij} is the distance between two particles indexed by i and j. Equation (2) was used to calculate the pair distribution functions reported in Fig. 2. To define clusters, particles were sorted according to their distance in the xy plane. A particle was assigned to a cluster if it was found within a threshold set to $1.5 \times d$, where d stands for a particle's diameter. These calculations were performed using the algorithm of Ref. [43], whereby allowing us to report cluster properties with time, see Fig. 4.

Simulations

Interparticle potentials were specified through the following model, inspired by work presented in Ref. [87]:

$$\phi(r \leq r_c) = -\epsilon\alpha(r_c, \sigma)\left(\left(\frac{\sigma}{r}\right)^2 - 1\right)\left(\left(\frac{r_c}{r}\right) - 1\right) \tag{3}$$

and $\phi(r \geq r_c) = 0$, where α is a normalizing prefactor so that the minimum of potential energy is $-\epsilon$; ϵ is the potential's depth. The potential reaches a minimum for $r \simeq 1.7\sigma$ when $r_c \gg \sigma$; σ is thus a parameter which sets the location of the minimum; and r_c is the range of the potential. ϵ, σ and r_c are parameters of the potential to be specified and that were calibrated using typical experimental data. The functional form of Equation (3) was chosen such that (i) the long-range decay of the potential scales like $1/r$, which corresponds to experimental expectations; (ii) one can set the range of interactions by choosing r_c separately from σ. A standard Euler-Maruyama scheme, implementing periodic boundary conditions, was used for integration. A further account of simulations is given in SI Sec. 4.

3. Results and discussion

Soft and long-range interparticle interactions under EDP

Herein, carboxyl-polystyrene particles (CB-PS) are subjected to low-frequency AC fields in parallel plate devices, see Fig. 1A. Fig. 1B shows 3D microscopy images of the electrochemical cell before and 130 s after applying an AC field of 5 V_{pp} and 100 Hz, viewed from the $x - z$ plane. The images combine emission intensity from a ratiometric dye (SNARF-1) collected at 580 nm (I_1, yellow orange), and at 640 nm (I_2, red), emission intensity from CB-PS particles (blue), as well as reflection from electrodes (green slabs). Once an AC field is applied, changes in color from SNARF-1 indicate substantial changes of pH throughout the electrochemical cell (see SI Sec. 1 and Ref. [86]). In response to non-monotonic pH profiles, particles migrate about 15 μm from the bottom electrode, where a maximum pH occurs [85,86]. Since particles experience vertical potential wells in the order of 100 k_BT, they remain within this levitated layer as long as the electric field is on. If loaded at sufficiently high particle densities (2.5% w/v), particles experience a transition from a disordered liquid into a colloidal crystal, as reported in [86] (Fig. 1C). Surprisingly, even under moderately dilute conditions (5×10^{-3}% w/v), particles form aggregates with high local order (Fig. 1D). This observation reveals that particles not only experience a large focusing potential in z-coordinate, but also pairwise interactions that induce aggregation under dilute conditions.

To reveal this interaction potential, we performed experiments in dilute conditions (5×10^{-4}% w/v) to avoid large aggregates. A pair of nearby interacting particles (a dimer) was first identified in the levitated layer (see SI-Movie 1). The position and trajectories of each particle were then extracted using particle tracking (Fig. 1E). Histograms of interparticle distance reveal that, through Brownian motion, particles sample a range of distances equivalent to 4 particle diameters ($d = 1.75$ μm), around a typical distance of $r_{min} \approx 4.6$ μm (Fig. 1F, and Fig. S3). The

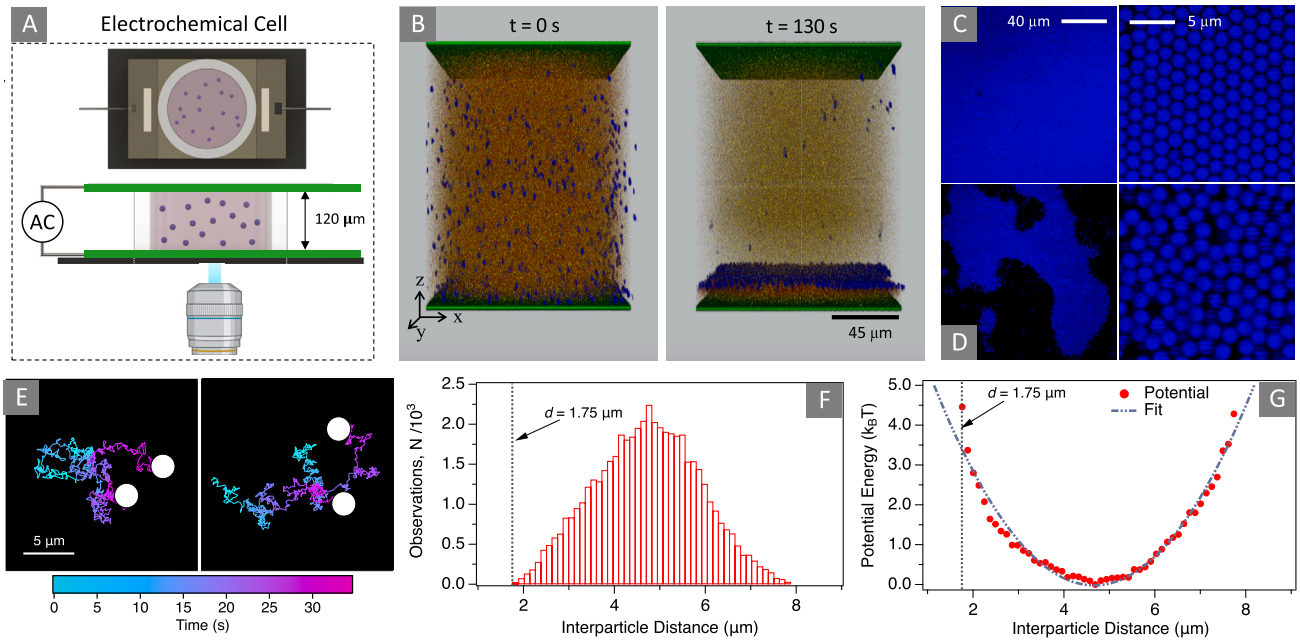

Fig. 1. EDP induces strong in-plane pairwise colloidal attraction. (A) Schematic of experimental setup. (B) Confocal images of volume between the electrodes (green slabs) before and 130 s after applying an AC field (100 Hz, 5 V_{pp}). CB-PS particles (blue) focus on a layer located tens of microns from the bottom electrode, where pH reaches a maximum value. (C) At high number densities (2.5% w/v), particles form crystals in the levitated layer. (D) Even at lower concentrations (5×10^{-3}% w/v), particles form aggregates with low crystalline order. (E) Trajectories of dimers in the levitated layer. (F) Histogram of interparticle distance for dimers, averaged over 4 different pairs totaling 50000 frames. Panel (G) shows the pairwise potential energy of dimers obtained by inverting the Boltzmann distribution. The fitted curve corresponds to $\phi(r) = k(r - r_{min})^2/2$, here $k = 3.3$ nN/m and $r_{min} = 4.6$ µm. Data in panels E-G was acquired from experiments under dilute conditions, using 1.75 µm CB-PS particles, 100 Hz and 5 V_{pp}. The concentration of particles was 5×10^{-4}% w/v. (For interpretation of the colors in the figure(s), the reader is referred to the web version of this article.)

positional information can be converted in this equilibrium regime into a potential energy landscape, $\phi(r)$, experienced by the particles, using the Boltzmann equation:

$$P(r) = Ae^{\phi(r)/(k_B T)}; \tag{4}$$

$P(r)$ is the probability of sampling interparticle distances of a given value r, whereas A is a normalization constant such that $\int_0^\infty P(r)dr = 1$, see also SI Sec. 2 for details. Fig. 1G shows the potential energy landscape calculated from the distribution in Fig. 1F [22,66]. Particles experience an attractive confining potential, with a depth of a few $k_B T$. This interaction has two important features. First, it is long-range (a few microns) compared to either electrostatic or van der Waals colloidal interactions (which extend over a few nanometers for micron-sized particles) [18,83,54]. It is important to note that particles experience an even larger range of interactions than we can resolve. In fact, due to the depth of the potential, events where particles move far from each other are rare and hard to sample. Second, the potential is soft, with a typical curvature corresponding to a spring constant $k \simeq 3 - 4$ nN/m (dictating an interparticle potential $\phi(r) = k(r - r_{min})^2/2$), orders of magnitude smaller than a polymer spring constant [65,16]. Interaction potentials of a few $k_B T$ are conducive to achieving well-organized structures through directed assembly [9]. Next, our goal is to understand the fundamental origin of this peculiar soft and long-range interaction potential under EDP.

Interactions originate from surface chemistry, through the establishment of a local pH gradient

To determine the origin of the interparticle potential, we repeat the experiment with different particles in moderately dilute conditions ($\approx 5 \times 10^{-3}$% w/v). The model systems are plain polysyrene (PS), silica and carboxyl-functionalized PS (CB-PS) particles. Images in Fig. 2A-F compare distributions of particles as soon as they arrive in the levitated layer and 300 s after. In stark contrast to CB-PS particles, neither plain PS nor silica particles form readily discernible structures over the course of the experiment. To gain further insight, we calculate, in the equilibrated state after 300 s, the radial pair distribution function $g(r)$, which quantifies the probability of finding a particle at a distance, r, from a reference particle (Fig. 2G-I). For plain PS, $g(r)$ resembles the behavior of an ideal hard-sphere gas since it remains constant with a value near 1; that is, positions of particles remain uncorrelated. For silica, $g(r)$ displays a sharp, rapidly decaying peak, reminiscent of a fluid-like structure with weak interactions. The positions of silica particles, albeit more correlated than for plain PS—as can be seen through small clusters in Fig. 2E—display only short ranged correlations. CB-PS particles display regular peaks, decaying in magnitude at larger distances, corresponding to ordering in dense fluid suspensions [29].

Since $g(r)$ is a manifestation of interparticle potentials [5,29], we can infer that attractive pairwise interactions are much smaller in range and magnitude for silica than for CB-PS, and nearly nonexistent for PS. Notice that mechanisms based on dipole-dipole or electrohydrodynamic flows cannot explain the formation of aggregates in our system. Dipole-dipole interactions would either tend to form chains aligned with the field or open 2D lattices [95,41]. Also, similar flow fields would be expected for dielectric particles of similar surface charge and diameter [64,39], as is the case here. However, PS, CB-PS, and silica particles display remarkably different behaviors. Therefore, differences in pair potentials must originate from another source. Surface chemistry of particles constitutes a plausible source since the dominant charged surface groups for PS, silica and CB-PS particles are ester sulfates, silanols and carboxylates, with dissociation constants (pKa) approximately equal to -1, 2.5, and 4, respectively.

To gain further insight into the effect of surface chemistry, we again dilute suspensions to a concentration of 5×10^{-4}% w/v to examine individual levitating particles. Fluorescence intensity from SNARF-1 surrounding each particle is then converted to pH values using ratiometric analysis, see Methods. The heat maps in Fig. 2J-L capture the spatial

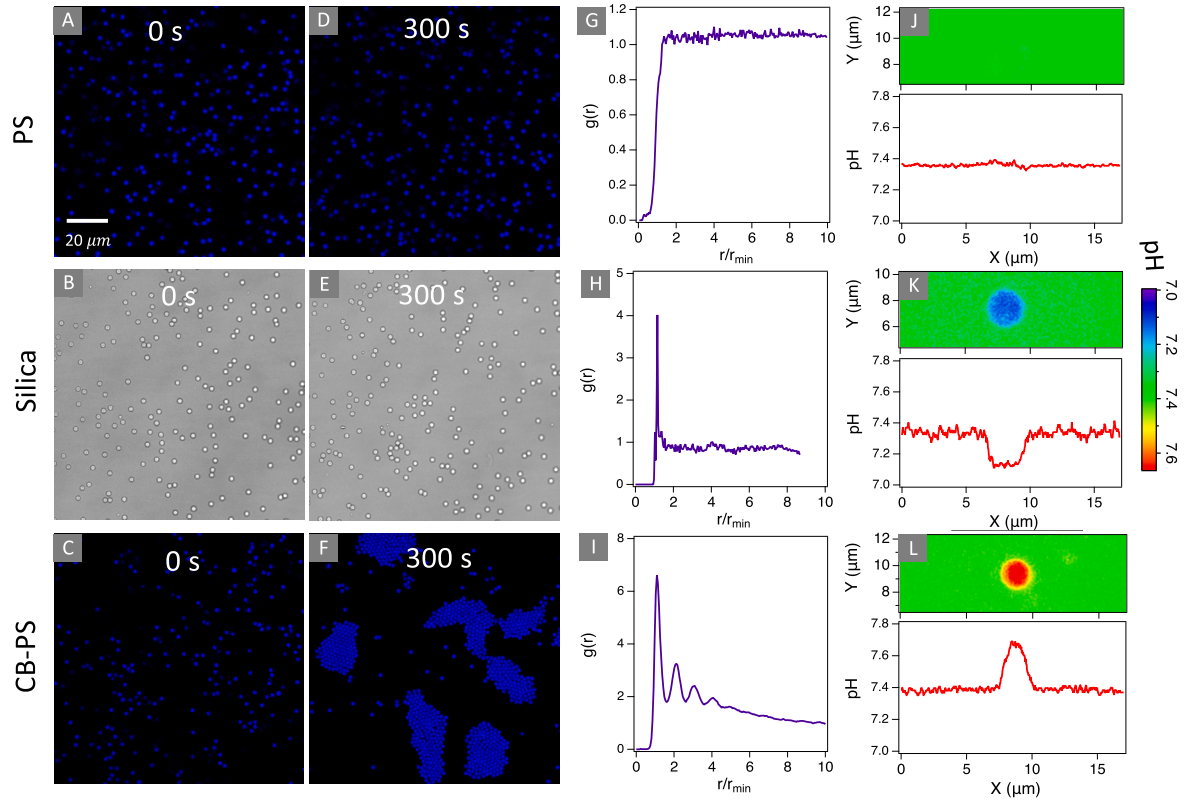

Fig. 2. Multiscale experiments reveal surface chemistry impacts the resulting interparticle potential under EDP. (A-C) Fluorescense and brightfield images of polystyrene (PS), Silica, and carboxyl-functionalized PS (CB-PS) particles immediately after reaching the levitated layer and (D-F) 300 s after. (G-I) Pairwise radial distribution function, $g(r)$, for each type of particle. (J-L) 2D heat maps indicating no change, decrease, or increase of pH around particles. Particles have similar sizes, zeta potentials and dielectric constants. A key difference between particles is the pK_a of dominant surface groups; for sulfate, silanol and carboxyl groups, the approximate values of pK_a are -1, 2.5, and 4. The applied field was 100 Hz and 5 V_{pp}. The $g(r)$ was obtained from averages over 165 frames, obtained after 300 s, for samples with concentrations of approximately 5×10^{-3}% w/v. Fluorescense images for PS and CB-PS particles are in false colors.

distribution of pH around a single particle; blue and red colors represent pH extrema corresponding to 7.0 and 7.6 respectively. Strikingly, a significant change of pH occurs near silica and CB-PS particles, while there is no observable change in pH near PS particles. The change in pH for silica particles is small, $\simeq 0.1$ units, and negative compared to that for CB-PS particles, which is large, $\simeq 0.3$ units, and positive. Although at the moment we cannot make any conclusive statements about the ultimate role of pKa, a correlation does appear between the observed changes in pH and $g(r)$: CB-PS particles display the largest change in pH and a strong tendency to aggregate, whereas PS particles show minimal change in pH, with no aggregation. Meanwhile, silica particles display intermediate behavior. Consequently, these observations suggest local pH gradients underlie the measured interaction potentials.

Local pH gradients mediate long-range interactions via diffusiophoresis

We hypothesize the interaction potential stems from diffusiophoretic flows, induced by local pH gradients surrounding the particles. In this case, each particle acts as a beacon. In our previous publication, we demonstrated that pH gradients along the z-axis cause migration of particles as well as focusing via diffusiophoresis (DP) [86]. Similarly, a target particle should respond to local chemical gradients induced by a neighboring particle; that is, particles should respond to multidimensional pH gradients as well. Generally, the diffusiophoretic velocity (U_{DP}) of a particle in a uniform and constant concentration gradient is given by,

$$U_{DP} = \mu_{DP} \nabla \ln c, \tag{5}$$

where the magnitude and sign of the diffusiophoretic mobility (μ_{DP}) depend on surface chemistry of particles, as well as on concentration (c) and properties of solutes [42].

Here, the measured pH gradient corresponds to a concentration gradient of H^+. The gradient in pH is likely the dominant contribution to the diffusiophoretic velocity, as it is the least concentrated species in solution, and $U_{DP} \propto \nabla \ln c = \nabla c / c$. In particular, the dye (0.1 mmol/L), is expected to yield only a minor correction to motion. In addition, Equation (5) provides a clue on the potential effect of a background electrolyte. Upon addition of an electrolyte, DP velocity to the focusing plane and towards each other would be reduced. These observations are supported by findings in our previous work [85]. It is important to note that aggregation is also observed either in the absence of SNARF-1 or in the presence of other dyes, such as sodium fluorescein; therefore, reported effects are not specific to the use of SNARF-1.

We can estimate the diffusiophoretic velocity U_{DP}. Since the in-plane pH gradient is symmetric around the particle, U_{DP} is also symmetric and depends only on interparticle distance r. We can thus approximate $\nabla \ln c \simeq \Delta \mathrm{pH} / \Delta r$, where ΔpH is the difference between the maximum pH value at the particle surface and bulk pH; Δr is the range over which this pH gradient extends. Based on experiments (Fig. 3A-B), we can take $\Delta \mathrm{pH} \simeq 0.1$ and $\Delta r \simeq 1$ μm. For our particles, the diffusiophoretic mobility can be calculated using expressions derived for the thin Debye layer limit (see SI Sec. 7), giving $\mu_{DP} \simeq 300\ \mu m^2/s$, which is consistent with other works [42,71,73]. However, our Debye length likely extends to tens of nanometers, since ion concentration is at most in the mmol/L range, due to the limited presence of dye and hydroxide ions. The prediction must thus be updated to account for a non-negligible Debye layer thickness, which can be estimated to reduce the diffusiophoretic mobility by about an order of magnitude [73,59]. Using $\mu_{DP} \simeq 10 - 100\ \mu m^2/s$,

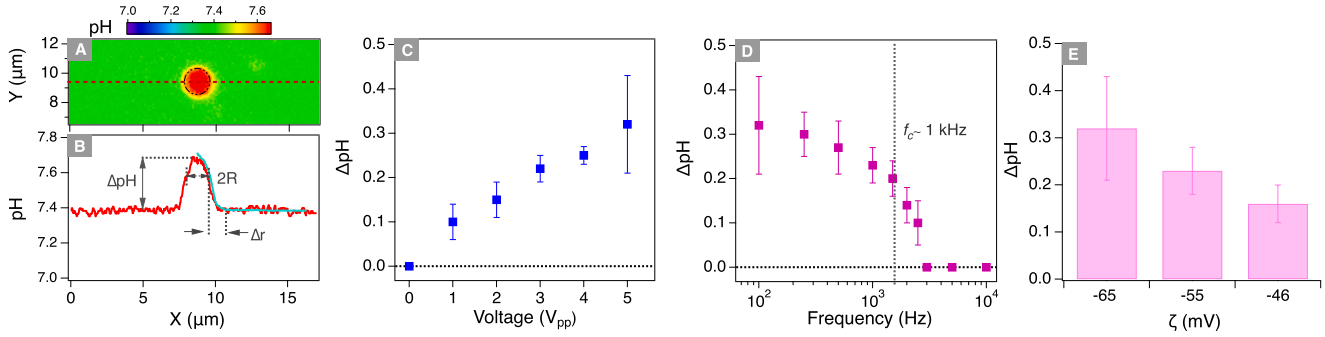

Fig. 3. Parameters of AC field and surface charge determine local pH gradients. (A-B) The same pH map and 1D pH profiles as in Fig. 2L; notice the outline of the particle in Panel A via a dashed line. The dashed horizontal line in Panel B provides the visual definition of ΔpH in Panel A. The cyan curve represents the radial pH profiles averaged over all polar angles (see SI, Fig. S5). Experimental conditions were as follows: C) 100 Hz, D) 5 V_{pp}, and E) 100 Hz, 5 V_{pp}. Error bars in Panels C-E represent the standard deviation of values from ten frames and ten different particles, for a total of 100 points. Zeta potential of particles was tuned by cross-linking PEG chains of different molecular weights to the carboxyl groups. Experiments in Panels C-E were performed using 5 μm CB-PS particles, for samples with concentrations of approximately 5×10^{-4}% w/v.

with $d = 2R$, we estimate with Eq. (5) $U_{DP}(R) \simeq 1 - 10$ μm/s at the particle's surface, which agrees with the range of measured interparticle velocities (Fig. S3). Given the potential role of concentration polarization and other complicating factors, a more detailed estimate of μ_{DP} is beyond the scope of our work.

Because fluid flow is incompressible, radially symmetric diffusiophoretic velocities should scale as $U_{DP}(r) \approx U_{DP}(R)\, R^2/r^2$ [49,51,50]. Such a diffusiophoretic flow field can be translated via $U_{DP}(r) \approx -D_0\phi'(r)/k_BT$ into a long-range effective potential $\phi(r) \sim (k_BT)R/r$, where D_0 represents the particle's diffusion coefficient. Note that diffusiophoresis is a force-free mechanism; therefore, the potential is merely an effective representation of the underlying flows [51,42]. Considering these scaling arguments, it is reasonable to conclude that local pH gradients induce aggregation of particles via diffusiophoresis. By inducing diffusiophoretic interactions, our work expands possibilities to control assembly and transport under AC electric fields. This is important because research on electrokinetics and field-directed assembly has so far been focused on dipole-dipole and hydrodynamic interactions.

External AC forcing sets local pH gradients around charged particles

We now investigate the origin of the local pH gradient surrounding CB-PS particles, which exhibit the strongest response to AC fields. To quantify the pH gradient, we extract pH profiles across the particle's equator (Fig. 3A-B). The disturbance of pH extends over 1.0 μm (Δr) from the surface of particles, making it of a similar length scale as the measured pairwise interaction potential. The profiles also provide ΔpH, the difference between the maximum pH value at the particle surface and bulk pH.

The properties of the external AC field—amplitude and frequency—set the values of ΔpH. Fig. 3C shows ΔpH for 5 μm CB-PS particles under different voltages. First, it is apparent that pH gradients do not appear in the absence of an applied electric field. Second, for voltages as low as 1 V_{pp}, pH changes substantially near a particle's surface, and increases with increasing voltage. Experiments at different frequencies (Fig. 3D) show pH gradients remain relatively constant between 0.1 and 1 kHz before rapidly decreasing at a cutoff frequency, $f_c \simeq 1$ kHz. This relaxation occurs at a similar frequency range for 1.75 μm particles (see SI, Fig. S10). In contrast, the range Δr where pH varies is much less sensitive to AC field parameters. Therefore, there is a wide frequency window to manipulate this phenomenon.

To discern the role of surface charge, we modify particles with poly(ethylene glycol) (PEG). The PEG chains controllably modify the amount of charges by covalently attaching to carboxyl groups. Consequently, the zeta potential of particles decreases as the size of attached PEG molecules increases. Fig. 3E indicates ΔpH increases with increasing magnitude of zeta potential. Local pH gradients thus depend on the number of carboxyl groups available. Lastly, observations in Fig. 3C-E provide strong evidence local changes in pH around particles are due to the electric field, and not to imaging artifacts—such as selective interactions between the dye molecules and particles.

These observations provide important insights. First, pH gradients only arise out of equilibrium, where the energy source corresponds to the finite electric field. Second, changes of ΔpH with zeta potential confirm the importance of available carboxyl groups. Therefore, we surmise charge regulation and dissociation equilibria of surface groups play important roles in the buildup of local pH profiles. Third, changes of ΔpH with frequency provide the characteristic time scale for the underlying phenomenon.

A diffusive process that matches the measured time scales is the relaxation of a polarized electrical double layer. When the double layer near a highly charged particle is driven far from equilibrium by an electric field, concentration gradients of electrolyte are established to compensate for the difference in conductivity near and far from the surface of particles; this phenomenon is called concentration polarization, CP. Concentration gradients of the neutral electrolyte extend beyond the double layer, have characteristic lengths in the order of a particle's diameter d, and their relaxation is dictated by diffusive timescales [33,20,38]. Therefore, the characteristic time (τ) for CP is dictated by the diffusion of ions across a distance roughly equal to the particle's diameter, d^2/D. Taking $d \simeq 2$ μm, and the diffusion coefficient for H^+, $D \simeq 9 \times 10^{-9}$ m^2/s, the characteristic time is thus $\tau = d^2/D \simeq 0.4$ ms, amounting to a frequency of $1/\tau \simeq 2.5$ kHz. Remarkably, this frequency agrees with the cut-off values observed in Fig. 3D and Fig. S10. The pH gradients observed near particles are likely a manifestation of the long-range concentration fields induced by CP. Furthermore, the increase of ΔpH with magnitude of zeta potential follows the expectation that a higher surface charge—higher surface conduction—leads to larger gradients. Consequently, we conjecture the observed ΔpH results from driving the double layer of dissociating groups far from equilibrium under highly non-monotonic global pH profiles.

Manipulating aggregation under EDP: from living clusters to chemotactic-like collapse

Linking changes in pH to interaction potentials widens the range and versatility of field-driven interactions beyond dipoles and electrohydrodynamic flows. Images in Fig. 4A and B report contrasting responses of CB-PS particles (1.75 μm) under similar forcing frequencies of 100 Hz, but different voltages. At 3 V_{pp} and moderate concentrations (5×10^{-2}% w/v), particles rapidly form aggregates (SI-Movie 2). Visually, the average aggregate size ceases to grow after some time. Particles in aggregates remain highly dynamic, with some coming in

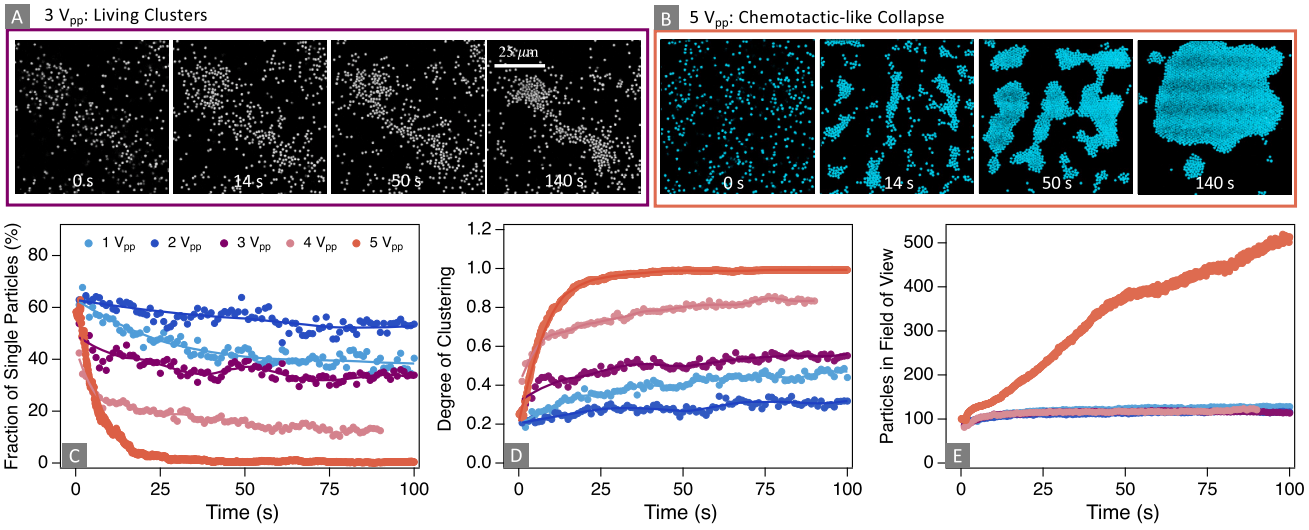

Fig. 4. Versatile nonequilibirum aggregation: from living clusters to chemotactic collapse. Sequence of images for 1.75 μm CB-PS particles, and 100 Hz: (A) at 3 V_{pp} demonstrating transient aggregation, and (B) at 5 V_{pp} demonstrating rapid coarsening. Characteristic horizontal black-cyan shades at 140 s correspond to waves on the assembled 2D micro sheet, with a wavelength around $\lambda \simeq 25$ μm. These waves represent slight variations in the vertical focusing position of particles. (C) Fraction of single particles defined as the number of single particles relative to the total number of particles in the field of view at a given time. (D) Degree of clustering, as introduced in Ref. [46], $\theta(t) = 1 - 1/\langle n_{clust}(t)\rangle$ where $\langle n_{clust}(t)\rangle$ is the mean cluster size at a given time. (E) Total number of particles in the field of view, rescaled by the number of particles in the field of view at the beginning of image acquisition. In (C-E), cluster properties are measured with increasing V_{pp}, at 100 Hz, with the legend shared across plots. Dots are data points and lines are guides for the eye corresponding to window averages. These experiments were performed with 1.75 μm CB-PS particles, with concentration of approximately 5×10^{-2}% w/v, and an average $\zeta = -65.0 \pm 3.1$ mV. For clarity, fluorescence images for 3 and 5 V_{pp} are reported in grayscale and false colors, respectively.

and out frequently. The aggregates resemble the behavior of the so-called "living clusters" seen in systems of self-propelled asymmetric particles [56,46,15,62,78,24,77,79].

In contrast, at large voltages (5 V_{pp}) the system does not reach a stationary state. After a few seconds, small, tight, clusters begin to form. These small clusters then attract more individual particles (14 s, Fig. 4B). The small clusters then aggregate with one another (50 s), in a similar way as the coarsening of droplets under Oswald ripening, eventually forming a single big cluster (140 s). Astoundingly, this cluster is not in a stationary state, as it keeps on attracting smaller clusters beyond the field of view (SI-Movie 3).

This tendency to collapse is reminiscent of the so-called "chemotactic collapse" displayed by bacteria or chemically-fueled, active Brownian particles (ABPs). Simulations of ABPs with local chemical fields have predicted collapsing behavior for small Péclet numbers, that is, when the propulsion velocity is slightly larger than the "Brownian velocity" [21, 56]. Here, the out-of-equilibrium aggregation phenomenon is radically different from ABPs. Following the discussion in Ref. [46], while *activity tends to break apart ABP clusters* via increased self-propulsion, *here activity is the driving force for aggregation* and thermal diffusion tends to break clusters. The Péclet number in our setting is $\mathrm{Pe} = U_{DP} R / D_0$ and must be large enough to observe collapse. With $U_{DP} \simeq 1 - 10$ μm/s, we find $\mathrm{Pe} \simeq 10 - 100$ which hints that activated aggregation can indeed be high enough to induce collapse in our experiments.

Paradoxically, while chemotactic behavior usually requires fuel consumption, here, there is no fuel! The driving force originates from the electric field that drives particle motion far from equilibrium. Measurements of pH reveal that ΔpH increases with the number of particles in a cluster, with a linear increase for clusters of up to $n_{clust} = 10$ particles (SI Fig. S8). Therefore, the driving force for aggregation increases with cluster size, thus facilitating the migration of smaller clusters to larger ones. This increase in driving force can be recovered by considering long-range potentials in simulations (SI Fig. S9). Such self-reinforcing interactions are characteristic of chemotaxis, hence our particles perform "artificial chemotaxis".

Cluster analysis in time provides more quantitative insights into the aggregation behavior (Fig. 4C-E). For each image, we group particles in clusters if their center-to-center distance is smaller than a cutoff distance ($3R$, see Methods). For weak interactions at voltages below 4 V_{pp}, all cluster parameters indicate the system reaches a steady state (Fig. 4C-E), where a finite fraction of single particles remains, Fig. 4C. The mean size of clusters is small, as given via the degree of clustering Fig. 4D, $\theta = 1 - 1/\langle n_{clust}\rangle$, where $\langle n_{clust}\rangle$ is the mean cluster size [46]. The total number of particles in the field of view remains constant within the noise level, Fig. 4E. In addition, cluster properties are rather noisy, indicating that clusters are transiently forming and splitting. We are thus in a dynamic steady state, characteristic of solid-liquid coexistence. In contrast, for high voltages, above 4 V_{pp}, the number of particles in the field of view increases with time (characteristic of a collapsing behavior), the fraction of single particles rapidly reaches 0 (meaning that after an initially short time, coarsening is the dominant growth mechanism), and the degree of clustering rapidly reaches 1 (characteristic of a solid). Our system thus allows one to easily manipulate various 2D aggregation regimes through field-driven interactions.

Versatility: single-particle beacons and the emergence of non-reciprocity

The versatility of our system is further illustrated by mixing particles of multiple sizes. Fig. 5A shows time-lapse images for 5 μm (blue) surrounded by 2 μm (red) CB-PS particles at the levitated layer (see also SI-Movie 4). Initially, small particles are located tens of microns away from a larger blue particle. After about 10 s, small particles begin to migrate towards the large one. Within 50 s, all particles indicated by green circles eventually become satellites of the large particle. Small particles remain mobile and continue to sample the space adjacent to large particles through Brownian motion. In the meantime, distant particles sometimes assemble into small transient clusters (as can be seen through a group of 3 at 50 s). By separately tracking the trajectory of a small particle near a large one, it becomes evident that small-large particles experience mutual attraction (SI Fig. S6).

To shed further light, we repeat our ΔpH investigation of Fig. 3 with particles of different sizes. We find that ΔpH increases with particle diameter (Fig. 5B). Since we have shown ΔpH is correlated to diffusiophoretic flows, these measurements suggest velocities around large blue

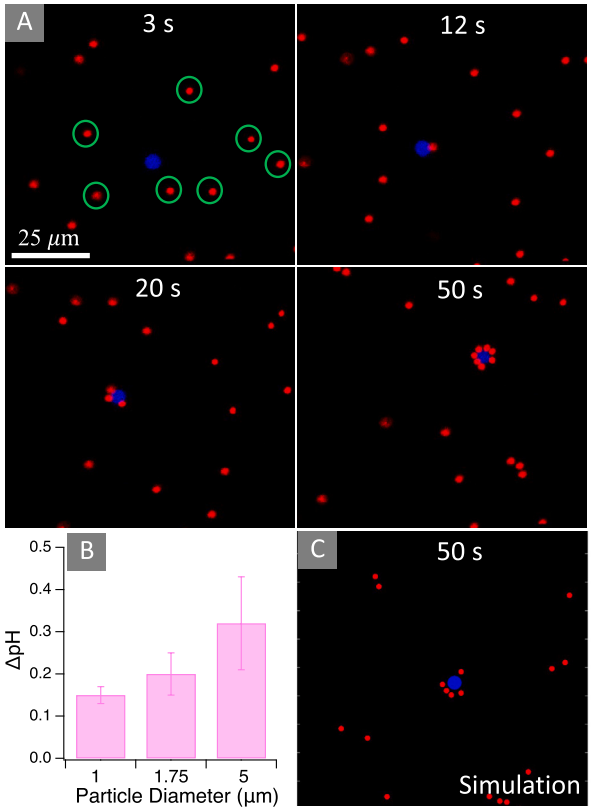

Fig. 5. Interparticle potential mediates capture of smaller particles. (A) Sequence of images for 5 μm (blue) surrounded by 2 μm (red) CB-PS particles at the levitated layer under 5 V_{pp} and 100 Hz. A large particle behaves as a beacon for smaller particles, indicated by green circles. (B) Size dependence of ΔpH. Error bars in Panel B represent the standard deviation of values from ten frames and ten different particles, for a total of 100 points. (C) Characteristic result of a Brownian dynamics simulation with interparticle potentials fitted from experimental data and initial configurations from (Panel A, 3s). The simulation domain is a square, with sides equal to 115 μm.

particles are greater than those surrounding small red particles. The size dependence of ΔpH thus manifests in a non-trivial way on the assembly of particles: large particles serve as levitating beacons for smaller particles. As a result, the attraction of red to blue is greater than that from blue to red or red to red, a key feature of non-reciprocal interactions. Non-reciprocal interactions were first demonstrated in active anisotropic colloids that locally consume fuel [76]. Since there is no fuel consumption here, it is surprising to see non-reciprocal interactions—and it hints at the generality of such a feature for systems with diffusiophoretic flows [36].

To confirm the underlying mechanism, we implement Brownian dynamics simulations of particles in 2D with non-reciprocal interactions under the form of standard potentials (see SI Sec. 4). The potentials are calibrated by using experimental data and by making reasonable assumptions when data is scarce. Starting from a similar configuration as in the experiment, we observe a similar beacon-like effect, where small red particles aggregate around the large blue particle over a short time scale of about 50 s (see Fig. 4C and SI-Movie 5). Therefore, interparticle potentials with minimal features are sufficient to reproduce the essential experimental observations. Electrodiffusiophoresis thus opens new possibilities to manipulate particles and their interactions with electric fields.

4. Conclusions

In this article, we have subjected charged particles to complex, non-monotonic, 3D chemical gradients externally generated by electric fields. Under these conditions, driving the electrical double layer far from equilibrium leads to local chemical fields, which in turn drive diffusiophoretic flows and versatile interparticle interactions. The observed interactions are long-ranged and easily tunable by the external field. Therefore, our findings have expanded the scope of interactions achievable under electric fields beyond dipole-dipole and electrohydrodynamic contributions [30,40]. This possibility, which was foreseen in the former Soviet Union by Gamayunov et al. [27], has rarely been explored. The insights from our work can inform the solution of long-standing problems in colloidal electrokinetics. For example, despite outstanding experimental and theoretical efforts, it has not been possible to explain how electrolyte [31,93,92,2] and surface chemistry [94] determine whether particles will separate or aggregate under low frequency AC fields near electrodes. Since the diffusiophoretic interactions discussed here are sensitive to surface chemistry and nature of electrolyte, they could play a significant role in inducing aggregation, calling for further theoretical and experimental investigations in that direction.

We envision these interactions will expand the tools for field directed assembly. To illustrate this point, we provided examples where a collection of simple particles behaves as a living crystal or experiences chemotactic collapse. Furthermore, particles of different diameters display non-reciprocal interactions [37,53], where small particles are more drawn towards large ones. Therefore, single large particles can behave as beacons towards smaller ones, which suggests a strategy to create materials with structural hierarchy. Notice that unlike active systems, particles display complex collective behavior without fuel consumption at their surface. On the other hand, such 2D, freely levitating systems naturally lend themselves to the study of collective dynamics of 2D colloidal suspensions without the need for a fluid-fluid interface, which can disturb interparticle interactions [11,12,55]. Diffusiophoretic engineering thus opens numerous opportunities for fundamental studies on colloidal suspensions beyond simple solutes and geometries [89,91,60].

CRediT authorship contribution statement

Carlos A. Silvera Batista: Writing – review & editing, Writing – original draft, Visualization, Software, Investigation, Funding acquisition, Formal analysis, Data curation, Conceptualization. **Kun Wang:** Investigation. **Hannah Blake:** Software, Formal analysis. **Vivian Nwosu-Madueke:** Investigation. **Sophie Marbach:** Writing – review & editing, Writing – original draft, Visualization, Software, Formal analysis, Conceptualization.

Declaration of competing interest

The authors declare that they have no known competing financial interests or personal relationships that could have appeared to influence the work reported in this paper.

Data availability

Data will be made available on request.

Acknowledgements

We thank Prof. Michael Bevan and Allec Pelliciotti for facilitating the MATLAB codes to calculate order parameters. We also thank Dr. Andrei S. Dukhin for pointing out important references. We acknowledge support from the National Science Foundation (NSF) under the CAREER award, Grant No. CBET-2239361. Elements of Fig. 1A were created using BioRender.com.

Appendix A. Supplementary material

Supplementary material related to this article can be found online at https://doi.org/10.1016/j.jcis.2024.08.004.

References

[1] B.M. Alessio, A. Gupta, Diffusiophoresis-enhanced Turing patterns, Sci. Adv. 9 (2023) eadj2457, https://doi.org/10.1126/sciadv.adj2457.

[2] S.M.H.H. Amrei, S.C. Bukosky, S.P. Rader, W.D. Ristenpart, G.H. Miller, Oscillating electric fields in liquids create a long-range steady field, Phys. Rev. Lett. 121 (2018) 185504, https://doi.org/10.1103/physrevlett.121.185504, https://journals.aps.org/prl/abstract/10.1103/PhysRevLett.121.185504.

[3] J.L. Anderson, Colloid transport by interfacial forces, Annu. Rev. Fluid Mech. 21 (61) (1989) 99, https://doi.org/10.1146/annurev.fl.21.010189.000425, http://www.annualreviews.org/doi/abs/10.1146/annurev.fl.21.010189.000425.

[4] J.L. Anderson, M.E. Lowell, D.C. Prieve, Motion of a particle generated by chemical gradients Part 1. Non-electrolytes, J. Fluid Mech. 117 (1982) 107–121, https://doi.org/10.1017/s0022112082001542.

[5] P. Attard, Thermodynamics and Statistical Mechanics, Academic Press, Amsterdam, 2002.

[6] A. Banerjee, T.M. Squires, Long-range, selective, on-demand suspension interactions: combining and triggering soluto-inertial beacons, Sci. Adv. 5 (2019) eaax1893, https://doi.org/10.1126/sciadv.aax1893.

[7] A. Banerjee, D.R. Vogus, T.M. Squires, Design strategies for engineering soluto-inertial suspension interactions, Phys. Rev. E 100 (2019) 052603, https://doi.org/10.1103/physreve.100.052603.

[8] A. Banerjee, I. Williams, R.N. Azevedo, M.E. Helgeson, T.M. Squires, Soluto-inertial phenomena: designing long-range, long-lasting, surface-specific interactions in suspensions, Proc. Natl. Acad. Sci. 113 (2016), https://doi.org/10.1073/pnas.1604743113, http://www.pnas.org/content/113/31/8612.full.

[9] M.A. Bevan, S.L. Eichmann, Optical microscopy measurements of kT-scale colloidal interactions, Curr. Opin. Colloid Interface Sci. 16 (2011) 149–157, https://doi.org/10.1016/j.cocis.2010.12.006.

[10] B. Bharti, O.D. Velev, Assembly of reconfigurable colloidal structures by multidirectional field-induced interactions, Langmuir 31 (2015) 7897–7908, https://doi.org/10.1021/la504793y.

[11] J. Bleibel, A. Domínguez, F. Günther, J. Harting, M. Oettel, Hydrodynamic interactions induce anomalous diffusion under partial confinement, Soft Matter 10 (2014) 2945–2948.

[12] J. Bleibel, A. Domínguez, M. Oettel, 3d hydrodynamic interactions lead to divergences in 2d diffusion, J. Phys. Condens. Matter 27 (2015) 194113.

[13] A.M. Brooks, M. Tasinkevych, S. Sabrina, D. Velegol, A. Sen, K.J.M. Bishop, Shape-directed rotation of homogeneous micromotors via catalytic self-electrophoresis, Nat. Commun. 10 (2019) 495, https://doi.org/10.1038/s41467-019-08423-7.

[14] E.O. Budrene, H.C. Berg, Complex patterns formed by motile cells of Escherichia coli, Nature 349 (1991) 630–633, https://doi.org/10.1038/349630a0.

[15] I. Buttinoni, J. Bialké, F. Kümmel, H. Löwen, C. Bechinger, T. Speck, Dynamical clustering and phase separation in suspensions of self-propelled colloidal particles, Phys. Rev. Lett. 110 (2013) 238301.

[16] F. Cui, S. Marbach, J.A. Zheng, M. Holmes-Cerfon, D.J. Pine, Comprehensive view of microscopic interactions between dna-coated colloids, Nat. Commun. 13 (2022) 2304.

[17] B. Derjaguin, S. Dukhin, A. Korotkova, Diffusiophoresis in electrolyte solutions and its role in mechanism of film formation from rubber latexes by method of ionic deposition, Kolloid. Zh. 23 (1961) 53.

[18] B. Derjaguin, L. Landau, Theory of the stability of strongly charged lyophobic sols and of the adhesion of strongly charged particles in solutions of electrolytes, Acta Physicochim. U.R.S.S. 14 (1941) 633–662.

[19] V.S. Doan, P. Saingam, T. Yan, S. Shin, A trace amount of surfactants enables diffusiophoretic swimming of bacteria, ACS Nano 14 (2020) 14219–14227.

[20] S. Dukhin, Non-equilibrium electric surface phenomena, Adv. Colloid Interface Sci. 44 (1993) 1–134, https://doi.org/10.1016/0001-8686(93)80021-3.

[21] F. Fadda, D.A. Matoz-Fernandez, R.v. Roij, S. Jabbari-Farouji, The interplay between chemo-phoretic interactions and crowding in active colloids, Soft Matter 19 (2023) 2297–2310, https://doi.org/10.1039/d2sm00957a.

[22] J.A. Fagan, Paul J. Sides, D.C. Prieve, Vertical oscillatory motion of a single colloidal particle adjacent to an electrode in an ac electric field, Langmuir 18 (2002) 7810–7820, https://doi.org/10.1021/la025721l.

[23] R. Fernández-Mateo, P. García-Sánchez, V. Calero, H. Morgan, A. Ramos, Stationary electro-osmotic flow driven by AC fields around charged dielectric spheres, J. Fluid Mech. 924 (2021) R2, https://doi.org/10.1017/jfm.2021.650.

[24] Y. Fily, M.C. Marchetti, Athermal phase separation of self-propelled particles with no alignment, Phys. Rev. Lett. 108 (2012) 235702.

[25] D. Florea, S. Musa, J.M.R. Huyghe, H.M. Wyss, Long-range repulsion of colloids driven by ion exchange and diffusiophoresis, Proc. Natl. Acad. Sci. 111 (2014) 6554–6559, https://doi.org/10.1073/pnas.1322857111, http://www.pnas.org/content/111/18/6554.full.

[26] L. Fu, C. Ybert, O. Bonhomme, L. Joly, A.L. Biance, Electrokinetic sweeping of colloids at a reactive magnesium oxide interface, Soft Matter 17 (2021) 8705–8711.

[27] N. Gamayunov, V. Murtsovkin, A. Dukhin, 1. Pair interaction of particles in electric fields, Kolloid. Zh. 48 (1986) 233–239.

[28] R. Guha, X. Shang, A.L. Zydney, D. Velegol, M. Kumar, Diffusiophoresis contributes significantly to colloidal fouling in low salinity reverse osmosis systems, J. Membr. Sci. 479 (2015) 67–76, https://doi.org/10.1016/j.memsci.2015.01.024.

[29] J.P. Hansen, I.R. McDonald, Theory of Simple Liquids: with Applications to Soft Matter, Academic Press, 2013.

[30] A.A. Harraq, B.D. Choudhury, B. Bharti, Field-induced assembly and propulsion of colloids, Langmuir 38 (2022) 3001–3016, https://doi.org/10.1021/acs.langmuir.1c02581.

[31] J.D. Hoggard, P.J. Sides, D.C. Prieve, Electrolyte-dependent pairwise particle motion near electrodes at frequencies below 1 kHz, Langmuir 23 (2007) 6983–6990, https://doi.org/10.1021/la070049j, http://pubs.acs.org/doi/abs/10.1021/la070049j.

[32] A. Joseph, C. Contini, D. Cecchin, S. Nyberg, L. Ruiz-Perez, J. Gaitzsch, G. Fullstone, X. Tian, J. Azizi, J. Preston, G. Volpe, G. Battaglia, Chemotactic synthetic vesicles: design and applications in blood-brain barrier crossing, Sci. Adv. 3 (2017) e1700362, https://doi.org/10.1126/sciadv.1700362.

[33] T. Kamsma, W. Boon, T. Ter Rele, C. Spitoni, R. Van Roij, Iontronic neuromorphic signaling with conical microfluidic memristors, Phys. Rev. Lett. 130 (2023) 268401.

[34] A. Kar, T.Y. Chiang, I.O. Rivera, A. Sen, D. Velegol, Enhanced transport into and out of dead-end pores, ACS Nano 9 (2015) 746–753, https://doi.org/10.1021/nn506216b.

[35] F. Katzmeier, B. Altaner, J. List, U. Gerland, F.C. Simmel, Emergence of colloidal patterns in ac electric fields, Phys. Rev. Lett. 128 (2022) 058002, https://doi.org/10.1103/physrevlett.128.058002, arXiv:2105.03590.

[36] B. Liebchen, A.K. Mukhopadhyay, Interactions in active colloids, J. Phys. Condens. Matter 34 (2021) 083002.

[37] S.A. Loos, S.H. Klapp, Irreversibility, heat and information flows induced by non-reciprocal interactions, New J. Phys. 22 (2020) 123051.

[38] J. Lyklema, Fundamentals of Interface and Colloid Science, vol. 2, Academic Press, San Diego, CA, 1995.

[39] F. Ma, S. Wang, D.T. Wu, N. Wu, Electric-field-induced assembly and propulsion of chiral colloidal clusters, Proc. Natl. Acad. Sci. 112 (2015) 6307–6312, https://doi.org/10.1073/pnas.1502141112, http://www.pnas.org/content/112/20/6307.

[40] F. Ma, X. Yang, H. Zhao, N. Wu, Inducing propulsion of colloidal dimers by breaking the symmetry in electrohydrodynamic flow, Phys. Rev. Lett. 115 (2015) 208302, https://doi.org/10.1103/physrevlett.115.208302, http://journals.aps.org/prl/abstract/10.1103/PhysRevLett.115.208302.

[41] J.R. Maestas, F. Ma, N. Wu, D.T. Wu, Electric-field-driven assembly of dipolar spheres asymmetrically confined between two electrodes, ACS Nano 15 (2021) 2399–2412, https://doi.org/10.1021/acsnano.0c04939.

[42] S. Marbach, L. Bocquet, Osmosis, from molecular insights to large-scale applications, Chem. Soc. Rev. 48 (2019) 3102–3144.

[43] Y. Marcon, Distance-based clustering of a set of xy coordinates: Version 1.5.0.0. MATLAB Central File Exchange, 2021.

[44] H. Massana-Cid, J. Codina, I. Pagonabarraga, P. Tierno, Active apolar doping determines routes to colloidal clusters and gels, Proc. Natl. Acad. Sci. 115 (2018) 10618–10623.

[45] J.J. McDermott, A. Kar, M. Daher, S. Klara, G. Wang, A. Sen, D. Velegol, Self-generated diffusioosmotic flows from calcium carbonate micropumps, Langmuir 28 (2012) 15491–15497, https://doi.org/10.1021/la303410w.

[46] B.M. Mognetti, A. Šarić, S. Angioletti-Uberti, A. Cacciuto, C. Valeriani, D. Frenkel, Living clusters and crystals from low-density suspensions of active colloids, Phys. Rev. Lett. 111 (2013) 245702.

[47] J.L. Moran, J.D. Posner, Phoretic self-propulsion, Annu. Rev. Fluid Mech. 49 (2017) 511–540, https://doi.org/10.1146/annurev-fluid-122414-034456.

[48] Y. Mu, L. Lei, J. Zheng, W. Duan, Z. Wang, J. Tang, Y. Gao, Y. Wang, Binary phases and crystals assembled from active and passive colloids, ACS Nano 16 (2022) 6801–6812, https://doi.org/10.1021/acsnano.2c01688.

[49] R. Niu, P. Kreissl, A.T. Brown, G. Rempfer, D. Botin, C. Holm, T. Palberg, J. De Graaf, Microfluidic pumping by micromolar salt concentrations, Soft Matter 13 (2017) 1505–1518.

[50] R. Niu, T. Palberg, Seedless assembly of colloidal crystals by inverted micro-fluidic pumping, Soft Matter 14 (2018) 3435–3442, https://doi.org/10.1039/c8sm00256h, http://pubs.rsc.org/en/content/articlelanding/2018/sm/c8sm00256h#!divAbstract.

[51] R. Niu, T. Palberg, T. Speck, Self-assembly of colloidal molecules due to self-generated flow, Phys. Rev. Lett. 119 (2017) 028001, https://doi.org/10.1103/physrevlett.119.028001, https://journals.aps.org/prl/abstract/10.1103/PhysRevLett.119.028001, arXiv:1702.08020.

[52] T.V. Nizkaya, E.S. Asmolov, O.I. Vinogradova, Theoretical modeling of catalytic self-propulsion, Curr. Opin. Colloid Interface Sci. 62 (2022) 101637, https://doi.org/10.1016/j.cocis.2022.101637, arXiv:2205.14357.

[53] S. Osat, R. Golestanian, Non-reciprocal multifarious self-organization, Nat. Nanotechnol. 18 (2023) 79–85.

[54] V.A. Parsegian, Van der Waals Forces: a Handbook for Biologists, Chemists, Engineers, and Physicists, Cambridge University Press, 2005.

[55] R.P. Peláez, F.B. Usabiaga, S. Panzuela, Q. Xiao, R. Delgado-Buscalioni, A. Donev, Hydrodynamic fluctuations in quasi-two dimensional diffusion, J. Stat. Mech. Theory Exp. 2018 (2018) 063207.

[56] O. Pohl, H. Stark, Dynamic clustering and chemotactic collapse of self-phoretic active particles, Phys. Rev. Lett. 112 (2014) 238303, https://doi.org/10.1103/physrevlett.112.238303, arXiv:1403.4063.

[57] D.C. Prieve, J.L. Anderson, J.P. Ebel, M.E. Lowell, Motion of a particle generated by chemical gradients. Part 2. Electrolytes, J. Fluid Mech. 148 (1984) 247–269, https://doi.org/10.1017/s0022112084002330.

[58] D.C. Prieve, S.M. Malone, A.S. Khair, R.F. Stout, M.Y. Kanj, Diffusiophoresis of charged colloidal particles in the limit of very high salinity, Proc. Natl. Acad. Sci. 116 (2019) 18257–18262.
[59] D.C. Prieve, R. Roman, Diffusiophoresis of a rigid sphere through a viscous electrolyte solution, J. Chem. Soc., Faraday Trans. 2: Mol. Chem. Phys. 83 (1987) 1287–1306.
[60] R.R. Raj, C.W. Shields, A. Gupta, Two-dimensional diffusiophoretic colloidal banding: optimizing the spatial and temporal design of solute sinks and sources, Soft Matter 19 (2023) 892–904, https://doi.org/10.1039/d2sm01549h, arXiv:2211.13795.
[61] B. Ramm, A. Goychuk, A. Khmelinskaia, P. Blumhardt, H. Eto, K.A. Ganzinger, E. Frey, P. Schwille, A diffusiophoretic mechanism for atp-driven transport without motor proteins, Nat. Phys. 17 (2021) 850–858.
[62] G.S. Redner, A. Baskaran, M.F. Hagan, Reentrant phase behavior in active colloids with attraction, Phys. Rev. E 88 (2013) 012305.
[63] R.A. Rica, M.Z. Bazant, Electrodiffusiophoresis: particle motion in electrolytes under direct current, Phys. Fluids 22 (2010) 112109, https://doi.org/10.1063/1.3496976, http://aip.scitation.org/doi/full/10.1063/1.3496976.
[64] W.D. Ristenpart, I.A. Aksay, D.A. Saville, Electrically driven flow near a colloidal particle close to an electrode with a faradaic current, Langmuir 23 (4071) (2007) 4080, https://doi.org/10.1021/la0628701.
[65] M. Rubinsten, R.H. Colby, Polymer Physics, 2003, United States of America.
[66] B. Rupp, I. Torres-Díaz, X. Hua, M.A. Bevan, Measurement of anisotropic particle interactions with nonuniform ac electric fields, Langmuir 34 (2018) 2497–2504, https://doi.org/10.1021/acs.langmuir.7b04066.
[67] J.M. Schurr, B.S. Fujimoto, L. Huynh, D.T. Chiu, A theory of macromolecular chemotaxis, J. Phys. Chem. B 117 (2013) 7626–7652, https://doi.org/10.1021/jp302587d, pMID: 23656252.
[68] S. SenGupta, C.A. Parent, J.E. Bear, The principles of directed cell migration, Nat. Rev. Mol. Cell Biol. 22 (2021) 529–547, https://doi.org/10.1038/s41580-021-00366-6.
[69] Z.M. Sherman, D. Ghosh, J.W. Swan, Field-directed self-assembly of mutually polarizable nanoparticles, Langmuir 34 (2018) 7117–7134, https://doi.org/10.1021/acs.langmuir.8b01135.
[70] S. Shim, Diffusiophoresis, diffusioosmosis, and microfluidics: surface-flow-driven phenomena in the presence of flow, Chem. Rev. 122 (2022) 6986–7009.
[71] S. Shim, J.K. Nunes, G. Chen, H.A. Stone, Diffusiophoresis in the presence of a ph gradient, Phys. Rev. Fluids 7 (2022) 110513.
[72] S. Shin, O. Shardt, P.B. Warren, H.A. Stone, Membraneless water filtration using CO2, Nat. Commun. 8 (2017) ncomms15181, https://doi.org/10.1038/ncomms15181, https://www.nature.com/articles/ncomms15181.
[73] S. Shin, E. Um, B. Sabass, J.T. Ault, M. Rahimi, P.B. Warren, H.A. Stone, Size-dependent control of colloid transport via solute gradients in dead-end channels, Proc. Natl. Acad. Sci. 113 (2016) 257–261, https://doi.org/10.1073/pnas.1511484112, http://www.pnas.org/content/113/2/257.
[74] S. Shin, P.B. Warren, H.A. Stone, Cleaning by surfactant gradients: particulate removal from porous materials and the significance of rinsing in laundry detergency, Phys. Rev. Appl. 9 (2018) 034012, https://doi.org/10.1103/physrevapplied.9.034012, https://journals.aps.org/prapplied/abstract/10.1103/PhysRevApplied.9.034012.
[75] C.A. Silvera Batista, H. Rezvantalab, R.G. Larson, M.J. Solomon, Controlled levitation of colloids through direct current electric fields, Langmuir 33 (2017) 10861–10867, https://doi.org/10.1021/acs.langmuir.7b00835, http://pubs.acs.org/doi/abs/10.1021/acs.langmuir.7b00835.
[76] R. Soto, R. Golestanian, Self-assembly of catalytically active colloidal molecules: tailoring activity through surface chemistry, Phys. Rev. Lett. 112 (2014) 068301.
[77] H. Stark, Artificial chemotaxis of self-phoretic active colloids: collective behavior, Acc. Chem. Res. 51 (2018) 2681–2688.
[78] J. Stenhammar, A. Tiribocchi, R.J. Allen, D. Marenduzzo, M.E. Cates, Continuum theory of phase separation kinetics for active brownian particles, Phys. Rev. Lett. 111 (2013) 145702.
[79] I. Theurkauff, C. Cottin-Bizonne, J. Palacci, C. Ybert, L. Bocquet, Dynamic clustering in active colloidal suspensions with chemical signaling, Phys. Rev. Lett. 108 (2012) 268303.
[80] V. Tricoli, G. Orsini, Electrodiffusiophoresis of a large-zeta-potential particle in weak fields, J. Phys. Condens. Matter 27 (2015) 415102, https://doi.org/10.1088/0953-8984/27/41/415102, http://iopscience.iop.org/article/10.1088/0953-8984/27/41/415102#cmaa0176s4.
[81] Z.R. Ulberg, A.S. Dukhin, Electrodiffusiophoresis - film formation in ac and dc electrical fields and its application for bactericidal coatings, Prog. Org. Coat. 18 (1990) 1–41, https://doi.org/10.1016/0033-0655(90)85001-e.
[82] D. Velegol, A. Garg, R. Guha, A. Kar, M. Kumar, Origins of concentration gradients for diffusiophoresis, Soft Matter 12 (2016) 4686–4703, https://doi.org/10.1039/c6sm00052e, http://pubs.rsc.org/en/content/articlelanding/2016/sm/c6sm00052e#!divAbstract.
[83] E.J.W. Verwey, J.T. Overbeek, Theory of the Stability of Lyophilic Colloids, Elsevier, Amsterdam, 1948.
[84] N. Wadhwa, H.C. Berg, Bacterial motility: machinery and mechanisms, Nat. Rev. Microbiol. 20 (2022) 161–173, https://doi.org/10.1038/s41579-021-00626-4.
[85] K. Wang, B. Behdani, C.A. Silvera Batista, Visualization of concentration gradients and colloidal dynamics under electrodiffusiophoresis, Langmuir 38 (2022) 5663–5673, https://doi.org/10.1021/acs.langmuir.2c00252.
[86] K. Wang, S. Leville, B. Behdani, C.A. Silvera Batista, Long-range transport and directed assembly of charged colloids under aperiodic electrodiffusiophoresis, Soft Matter 18 (2022) 5949–5959, https://doi.org/10.1039/D2SM00631F.
[87] X. Wang, S. Ramírez-Hinestrosa, J. Dobnikar, D. Frenkel, The Lennard-Jones potential: when (not) to use it, Phys. Chem. Chem. Phys. 22 (2020) 10624–10633.
[88] Z. Wang, Z. Wang, J. Li, C. Tian, Y. Wang, Active colloidal molecules assembled via selective and directional bonds, Nat. Commun. 11 (2020) 2670, https://doi.org/10.1038/s41467-020-16506-z.
[89] P.B. Warren, Non-faradaic electric currents in the Nernst-Planck equations and nonlocal diffusiophoresis of suspended colloids in crossed salt gradients, Phys. Rev. Lett. 124 (2020) 248004, https://doi.org/10.1103/physrevlett.124.248004, arXiv:1912.06016.
[90] P.B. Warren, S. Shin, H.A. Stone, Diffusiophoresis in ionic surfactants: effect of micelle formation, Soft Matter 15 (2019) 278–288, https://doi.org/10.1039/c8sm01472h, https://pubs.rsc.org/en/Content/ArticleLanding/2018/SM/C8SM01472H#!divAbstract.
[91] I. Williams, P.B. Warren, R.P. Sear, J.L. Keddie, Colloidal diffusiophoresis in crossed electrolyte gradients: experimental demonstration of an “action-at-a-distance” effect predicted by the Nernst-Planck equations, Phys. Rev. Fluids 9 (2024) 014201.
[92] C.L. Wirth, P.J. Sides, D.C. Prieve, Electrolyte dependence of particle motion near an electrode during ac polarization, Phys. Rev. E 87 (2013), https://doi.org/10.1103/physreve.87.032302.
[93] T.J. Woehl, K.L. Heatley, C.S. Dutcher, N.H. Talken, W.D. Ristenpart, Electrolyte-dependent aggregation of colloidal particles near electrodes in oscillatory electric fields, Langmuir 30 (2014) 4887–4894, https://doi.org/10.1021/la4048243.
[94] X. Yang, S. Johnson, N. Wu, The impact of Stern-layer conductivity on the electrohydrodynamic flow around colloidal motors under an alternating current electric field, Adv. Intell. Syst. 1 (2019) 1900096, https://doi.org/10.1002/aisy.201900096.
[95] A. Yethiraj, A.v. Blaaderen, A colloidal model system with an interaction tunable from hard sphere to soft and dipolar, Nature 421 (2003) 513–517, https://doi.org/10.1038/nature01328.
[96] J. Zheng, J. Chen, Y. Jin, Y. Wen, Y. Mu, C. Wu, Y. Wang, P. Tong, Z. Li, X. Hou, J. Tang, Photochromism from wavelength-selective colloidal phase segregation, Nature 617 (2023) 499–506, https://doi.org/10.1038/s41586-023-05873-4.